Tunable Electronic Properties of Two-Dimensional Transition Metal Dichalcogenide Alloys: A First-Principles Prediction

Jinyang Xi,[†] Tianqi Zhao,[†] Dong Wang,*,[†] and Zhigang Shuai*,[†,‡]

[†]MOEKey Laboratory of Organic OptoElectronics and Molecular Engineering, Department of Chemistry, Tsinghua University, 100084 Beijing, People's Republic of China

[‡]Key Laboratory of Organic Solids, Beijing National Laboratory for Molecular Science (BNLMS), Institute of Chemistry, Chinese Academy of Sciences, 100190 Beijing, People's Republic of China

S Supporting Information

ABSTRACT: We investigated the composition-dependent electronic properties of two-dimensional transition-metal dichalcogenide alloys ($W_xMo_{1-x}S_2$) based on first-principles calculations by applying the supercell method and effective band structure approximation. It was found that hole effective mass decreases linearly with increasing W composition, and electron effective mass of alloys is always larger than that of their binary constituents. The different behaviors of electrons and holes in alloys are attributed to the fact that metal d-orbitals have different contributions to conduction bands of MoS_2 and WS_2 but almost identical contributions to valence bands. We examined the conduction polarity of $W_xMo_{1-x}S_2$ monolayer alloys with four metal electrode materials (Au, Ag, Cu, and Pd). It suggests the main carrier type for transport in transistors could change from electrons to holes as W composition increases if high work function metal contacts were used. The tunable electronic properties of two-dimensional transition-metal dichalcogenide alloys make them attractive for electronic and optoelectronic applications.

SECTION: Plasmonics, Optical Materials, and Hard Matter
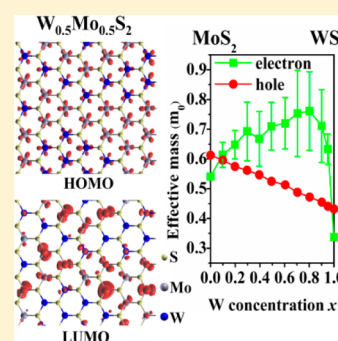
Recently, progress, challenges, and opportunities in two-dimensional (2D) materials beyond graphene have been reviewed.[1] Single-layered transition-metal dichalcogenides (TMDs) as a novel class of 2D materials have caught our attention. The versatile chemistry and unique electrical and optical properties of TMDs make them attractive for a variety of applications ranging from hydrogen evolution, energy storage, to transistors, photodetectors, and electroluminescent devices.[1−6] Bulk TMDs are van der Waals solids with a layered structure similar to graphite: within each layer, a plane of metal atoms is sandwiched between, and covalently bonded to two planes of chalcogen atoms. They can be exfoliated mechanically or chemically into mono- or few-layered TMDs.[5−7] Synthesis of large-area ultrathin MoS_2 layers using chemical vapor deposition (CVD) has also been demonstrated.[8−11] Interestingly, TMDs such as MoS_2 and WS_2 exhibit a transition from an indirect bandgap semiconductor in the bulk to a direct bandgap semiconductor in the monolayer, which has been manifested by enhanced photoluminescence in the monolayer[5,12] as well as theoretical band structure calculations.[13] In contrast to the semimetallic graphene sheet,[14] the MoS_2 monolayer has a sizable bandgap (~1.8 eV),[5] and field-effect transistors (FETs) made of it show high room-temperature current on/off ratios (>10^7).[6,15] It exhibits n-type conductivity with an electron effective mass ~$0.48m_0$,[16] and room-temperature mobility >200 cm^2 V^{-1} s^{-1} in top-gated transistors with a high-dielectric gate,[6,17] benefited from screening of impurity scatterings by the dielectric engineering.[18] Also, first-principles calculations

predicted a room-temperature electron mobility of 130−420 cm^{2}V^{-1}s^{-1}, and the charge transport behavior in it was found to be dominated by optical phonon scatterings via intra- and intervalley scattering mechanism and Fröhlich interaction.[19,20] With carrier mobility comparable to Si, 2D semiconducting TMDs have been suggested for flexible and transparent electronic applications.

The unique properties of semiconducting TMD monolayers can be extended by alloying two compounds of different electronic properties. The transition metal atomic mixing in $W_xMo_{1-x}S_2$ single layers has been visualized and quantified recently.[21] We have shown in an earlier study that bandgaps of atomically thin TMD alloys are tunable by mixing MoS_2 and WS_2 and controlling the composition of alloys.[22] TMD monolayer alloys have opened new possibilities for band structure engineering and electronic and optoelectronic applications. The fundamental electronic properties of these 2D alloys form the physical basis for the fabrication of FET devices based on them and provide guidance for the selection of metal electrode materials. Both theoretical predictions of electronic properties and device characterization of charge transport behaviors have been performed for pure and single-layered TMDs. Among these, MoS_2 is most extensively studied. However, investigations on the electronic properties of 2D

TMD alloys are still lacking. In this Letter, we focus on the composition-dependent electronic properties of 2D alloys $W_xMo_{1-x}S_2$ and report tunable effective masses of charge carriers and conduction polarity in 2D TMD alloys $W_xMo_{1-x}S_2$ based on first-principles predictions.

The electronic structures of $W_xMo_{1-x}S_2$ monolayer alloys were determined first-principly by applying the supercell method and the effective band structure (EBS) approximation.[23] Although disordered alloys $A_{1-x}B_xC_2$ constructed by ordered constituents AC_2 and BC_2 are inevitably associated with loss of long-range order, and then automatic loss of the concept of band structure $E(\mathbf{k})$, the language of effective band structure continues to be enormously useful for phenomenologically describing and discussing electronic properties of random alloys. The EBS approximation maps the eigenvalues obtained from large supercell calculations into an effective band structure in the primitive cell, and is able to recover an approximate $E(\mathbf{k})$ for alloys. The experimental observables for alloys are very often interpreted in terms of such quantities as the effective mass, which can be readily derived from the band dispersion relations.

In all the calculations carried out throughout this work, we employed the density functional theory (DFT) with the exchange-correlation functional of local density approximation (LDA)[24] and the projector augmented wave (PAW)[25,26] formalism as implemented in the Vienna ab initio simulation package (VASP).[27,28] The energy cutoff for plane-wave expansion was set to 400 eV. A $\mathbf{k}$-grid of $21 \times 21 \times 1$ was used for the Brillouin zone of primitive cell, and the energy convergence criteria for the electronic self-consistent cycle was set to 10^{-5} eV. The spin−orbit coupling (SOC) effect leads to a significant splitting at the top of the valence band in MoS_2 and WS_2.[29,30] It was not considered in our calculations because the band gap of WS_2 predicted with SOC included is smaller than that of MoS_2, which is contradictory with the experimental observations.[22] As seen from Tables S1 and S2 in the Supporting Information (SI), whether SOC is considered does not change the trend of effective mass and the character of highest occupied molecular orbital (HOMO) and lowest unoccupied molecular orbital (LUMO) in MoS_2 and WS_2. Most semiconductor alloys $A_{1-x}B_xC_2$ show a nonlinear bowing dependence of its bandgap $E_g(x)$ with the alloy composition x, and bandgap bowing can be decomposed into three contributions:[31,32] (i) volume deformation, (ii) charge exchange, and (iii) structural relaxation. Since the lattice constants of bulk $2H$-MoS_2 (3.160 Å) and bulk $2H$-WS_2 (3.153 Å) are close to each other,[33] here we study solely the influence of charge exchange on the electronic structure of $W_xMo_{1-x}S_2$ monolayer alloys in which the metal coordination is trigonal prismatic. We have shown that the band gap bowing coefficient obtained from the first-principles calculations that take into account charge exchange effect only, coincides with the experimental value.[22] This is a manifestation that influences of volume deformation and structural relaxation are insignificant in $W_xMo_{1-x}S_2$ alloys. The lattice constant in our calculations was taken from the crystal structure of bulk $2H$-MoS_2, and the interlayer distance was set to 10 Å in order to eliminate interlayer interactions. To model $W_xMo_{1-x}S_2$ monolayer alloys, eight random configurations of metal atoms within a 9×9 supercell (including $3 \times 9 \times 9 = 243$ atoms) were set up for each W composition x, with $x = 0.099$, 0.198, 0.296, 0.395, 0.494, 0.605, 0.704, 0.802, 0.901, and 0.951. For pure MoS_2 and WS_2, calculations were based on the supercell

approach too. For each configuration at a specified W composition x, Mo atoms were randomly replaced by W atoms using a random number generation method. To check the convergence with respect to supercell size and number of configurations, calculations with 6×6 supercell, eight random configurations at $x = 0.5$ and with 9×9 supercell, 16 random configurations at $x = 0.2$ were also performed. The results included in Table S3 of the SI show that our choice of 9×9 supercell and eight random samples is reasonable. Figure 1 shows a 9×9 supercell of $W_{0.5}Mo_{0.5}S_2$ monolayer alloys in the $x−y$ and $x−z$ planes, respectively.
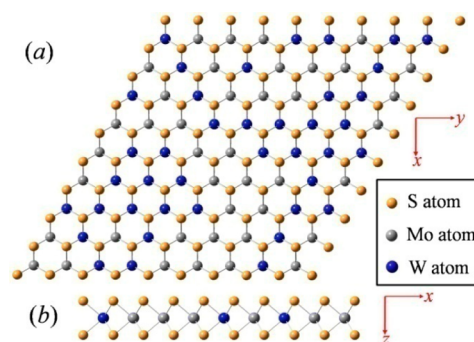

Figure 1. Structure of a 9×9 supercell of $W_{0.5}Mo_{0.5}S_2$ (including 40 W atoms and 41 Mo atoms) in the (a) $x−y$ plane and (b) $x−z$ plane. The orange spheres represent S atoms, and the gray and blue spheres represent Mo and W atoms, respectively.

To obtain the EBS of random alloys, we need to transform eigenstates in the large supercell into an effective band structure in the primitive cell. This unfolding procedure can be described by a spectral function (SF) of the continuous energy variable E:

$$A(\mathbf{k}, E) = \sum_{m,n} |\langle \mathbf{K}m|\mathbf{k}n\rangle|^2 \delta(E_m - E) \tag{1}$$

where $|\mathbf{k}n\rangle$ and $|\mathbf{k}m\rangle$ (n and m are band indices) are the Bloch states in the primitive cell and supercell, respectively. With the SF determined for a set of $|\mathbf{k}\rangle$ (a given $|\mathbf{k}\rangle$ is mapped precisely into a single $|\mathbf{K}\rangle$ according to the geometry and symmetry of the supercell and its primitive cell) and over a wide range of energies, we subsequently constructed the EBS of random alloys. For the supercell of ordered systems, SF is a set of δ-functions because the symmetry does not change when going from the primitive cell to the supercell. However, for alloys, the symmetry is broken, and different local environments in the alloys are reflected by a finite width of SF defined in eq 1. The detailed description about the EBS method can be found in ref 23. The energy $E(\mathbf{k})$ at which the SF shows a peak value and closest to the band edge was chosen for the parabolic fitting to obtain the effective mass. Also, for the parabolic fitting along each direction, we chose five $E(\mathbf{k})$ with $\mathbf{k}$ in the vicinity of the K-point. The EBS along high symmetry lines for a random configuration of $W_{0.5}Mo_{0.5}S_2$ monolayer alloys is plotted in Figure 2. It can be seen that the conduction band (CB) has a broader SF than the valence band (VB) (see the light-blue shaded areas of Figure 2), which reflects different influences of local environments on the CB and VB of the alloys. The EBS of alloys also shows that $W_xMo_{1-x}S_2$ monolayer alloys are direct band gap semiconductors, with band edges of CB and VB coinciding at the K-point. However, the energy difference between the K- and Y-point (located in the midway between Γ-
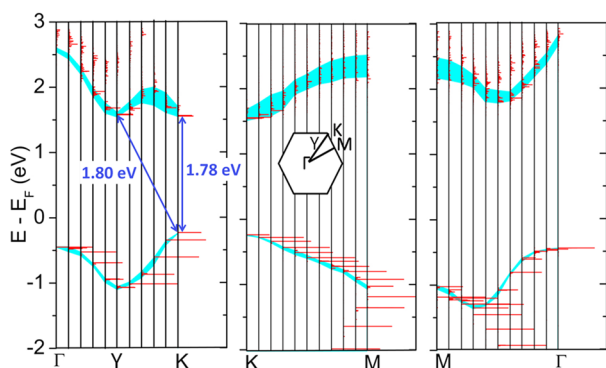
Figure 2. Effective band structure of one of configurations of $W_{0.5}Mo_{0.5}S_2$ alloys. It is a direct band gap (E_{gap} = 1.78 eV). The different **k** vectors in the primitive cell are represented by a thin vertical line. The red areas represent the spectral functions $A(\mathbf{k}, E)$ at each **k** point, and the blue shaded areas represent the width of $A(\mathbf{k}, E)$ for CB and VB. The inset displays the first Brillouin zone of the primitive cell with three high symmetry points Γ, K, and M, as well as a special Y-point along the Γ−K direction.

Figure 3. Composition-dependent effective masses of electrons and holes for $W_xMo_{1-x}S_2$ monolayer alloys. The blue square represents the effective mass of electrons, while the red circle represents that of holes. The error bars represent the standard deviation of electron (hole) effective masses calculated for eight random configurations. m_0 is the bare electron mass.

and K-points) is only 20 meV for the CB of $W_{0.5}Mo_{0.5}S_2$ (for the CB of MoS_2 and WS_2 monolayer, we found the value of 74 and 25 meV, respectively). This indicates that, in addition to the major intravalley scattering in the K-valley, the intravalley scattering in the Y-valley and intervalley scattering between K- and Y-valleys also play an important role in the electron transport.[20] Here, we focus on the carrier effective mass in the K-valley. The conduction band structure is not very well-defined compared to the valence band structure, as can be seen from the broader SF near the K-valley. The similar width of SF, ~ 0.25 eV, was also observed for the valence band of $In_{0.5}Ga_{0.5}N$ near the Γ-point in the original EBS paper of Zunger.[23] The large variation in the conduction band structure for different configurations and the subsequent parabolic fitting give rise to large error bars in the electron effective mass. According to $E(\mathbf{k}) = E_0 + \hbar^2\mathbf{k}^2/2m^*$, where E_0 is the band energy at the K-point and **k** is the wave-vector relative to the K-point, we calculated the electron and hole effective masses of eight random configurations at each W composition, along both K−Γ and K−M directions, and then obtained the effective mass of a specific configuration as $m^*_{eff} = (m^*_{K-\Gamma}m^*_{K-M})^{1/2}$ to account for the band anisotropy. Finally, the effective mass $\overline{m}^*_{e(h)}$ averaged over eight configurations and the corresponding error bars were obtained for different compositions of $W_xMo_{1-x}S_2$ monolayer alloys, as plotted in Figure 3 and summarized in Table 1. The electron and hole effective masses of individual configuration at different W compositions were provided in Table S4 in the SI. The results mainly show that (i) both electron and hole effective masses of MoS_2 and WS_2, as well as the hole effective mass of alloys are almost isotropic, while the electron effective mass along the K−Γ direction of alloys differs noticeably from that along the K−M direction; (ii) the electron effective mass of MoS_2 is $0.54m_0$ (m_0 is the bare electron mass), which is close to the value reported in the literatures,[15,16] and both electron and hole effective masses of WS_2 are smaller than those of MoS_2, suggesting that WS_2 monolayer has better transport properties; (iii) the electron effective mass of random alloys is always larger than that of MoS_2 and WS_2, and the error bars are large, which indicates that the electron effective mass depends strongly on the distribution of metal atoms in the alloys. The large electron
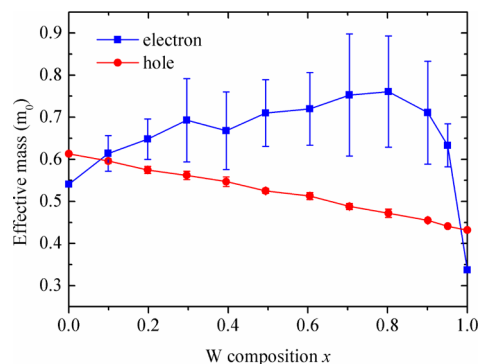
effective masses of $W_xMo_{1-x}S_2$ have a negative effect on electron transport; (iv) in contrast to the electron effective mass, the hole effective mass decreases linearly with increasing W composition, and the error bars are small, indicating little influence of metal configurations on the hole effective mass; (v) the hole effective mass is always smaller than the electron effective mass in $W_xMo_{1-x}S_2$ monolayer alloys for all W compositions x (except for x = 0 and 1).

To understand these results, we examined the absolute energy level (Table S5 of the SI), the composition (Figure 4), and charge density distribution (Figure S1 of the SI) of the frontier orbitals in MoS_2, $W_{0.5}Mo_{0.5}S_2$, and WS_2, respectively. The absolute energy levels of HOMO and LUMO in MoS_2 and WS_2 were determined by the method of vacuum level calibration.[34,35] To obtain the vacuum level, we recalculated the band energies of MoS_2 and WS_2 with an interlayer distance of 30 Å (see Figure S2 and eq S1 in the SI for more details). It is found that the HOMO and LUMO levels of WS_2 are both higher than those of MoS_2, which is easy to understand because W is heavier than Mo. The projected density-of-states (PDOS) analysis for the frontier orbitals were provided in Figure 4 and Table S5 of the SI. As seen, the metal contribution to HOMO is d_{xy} and $d_{x^2-y^2}$ orbitals for both MoS_2 and WS_2; by contrast, the metal contribution to LUMO is d_{z^2} orbitals for MoS_2 but d_{xy}, $d_{x^2-y^2}$, and d_{z^2} orbitals for WS_2. Based on the frontier orbital analysis, we explain different behaviors of electrons and holes in $W_xMo_{1-x}S_2$ monolayer alloys as follows: (i) W atoms directly participate in the formation of HOMO in alloys due to identical orbital compositions for MoS_2 and WS_2. Meanwhile, the electronic coupling in WS_2 is stronger than that in MoS_2, so that the hole effective mass of WS_2 is smaller. These two facts together lead to a linear decrease of the hole effective mass with increasing W composition; (ii) due to different compositions of LUMO for MoS_2 and WS_2, and lower LUMO level of MoS_2, mixing of W atoms into MoS_2 only slightly reduces the electronic coupling and increases the electron effective mass. On the other side, mixing of Mo atoms into WS_2 leads to a sudden increase in the electron effective mass because the electronic properties of LUMO of alloys is mainly determined by Mo atoms due to the lower LUMO level of MoS_2. From the above analysis, it is clear that 2D $W_xMo_{1-x}S_2$ alloys always have a larger electron effective mass than either MoS_2 or WS_2, and alloying could not improve the electron mobility in n-type

287

dx.doi.org/10.1021/jz402375s | J. Phys. Chem. Lett. 2014, 5, 285−291

Table 1. The Electron (Hole) Effective Mass (in m_0) along the K–Γ ($m_{K-\Gamma}^*$) and K–M (m_{K-M}^*) Directions as well as the Geometric Mean $m_{eff}^* = (m_{K-\Gamma}^* m_{K-M}^*)^{1/2}$ for $W_xMo_{1-x}S_2$ Alloys with Different W Composition x^a

x	0.0	0.099	0.198	0.296	0.395	0.494	0.605	0.704	0.802	0.901	0.951	1.0
						electron						
$m_{K-\Gamma}^*$	0.537	0.65 (0.06)	0.70 (0.08)	0.78 (0.19)	0.73 (0.16)	0.81 (0.13)	0.81 (0.12)	0.87 (0.26)	0.86 (0.20)	0.81 (0.15)	0.73 (0.07)	0.339
m_{K-M}^*	0.546	0.58 (0.03)	0.60 (0.04)	0.61 (0.06)	0.61 (0.05)	0.63 (0.06)	0.64 (0.10)	0.65 (0.10)	0.67 (0.14)	0.63 (0.12)	0.55 (0.05)	0.335
m_{eff}^*	0.541	0.61 (0.04)	0.65 (0.05)	0.69 (0.10)	0.67 (0.09)	0.71 (0.08)	0.72 (0.09)	0.75 (0.15)	0.76 (0.13)	0.71 (0.12)	0.63 (0.05)	0.337
						hole						
$m_{K-\Gamma}^*$	0.591	0.574 (0.005)	0.567 (0.006)	0.555 (0.015)	0.541 (0.018)	0.518 (0.009)	0.498 (0.011)	0.480 (0.006)	0.464 (0.005)	0.443 (0.001)	0.432 (0)	0.421
m_{K-M}^*	0.635	0.619 (0.009)	0.583 (0.015)	0.569 (0.016)	0.553 (0.019)	0.532 (0.008)	0.528 (0.020)	0.496 (0.016)	0.480 (0.018)	0.467 (0.006)	0.452 (0)	0.443
m_{eff}^*	0.613	0.596 (0.006)	0.575 (0.009)	0.562 (0.010)	0.547 (0.011)	0.525 (0.006)	0.513 (0.008)	0.488 (0.008)	0.472 (0.010)	0.455 (0.004)	0.441 (0)	0.432

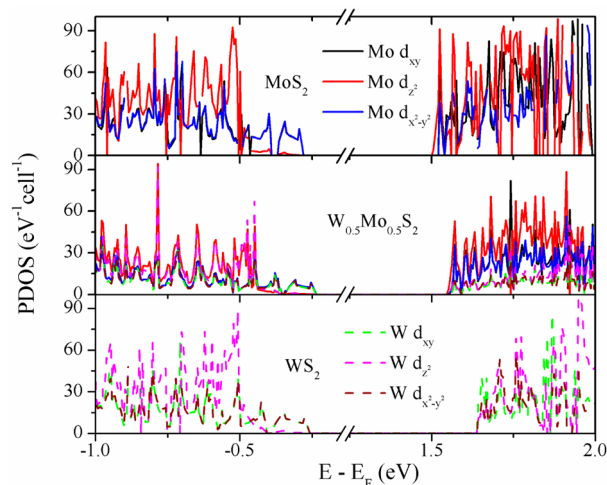$^a m_0$ is the bare electron mass. The number in the bracket is the error bar.

Figure 4. Projected density-of-states for the valence and conduction bands of MoS_2, $W_{0.5}Mo_{0.5}S_2$, and WS_2, respectively. The 9 × 9 supercell was used for the calculations and analysis. It is noted that the composition of the valence bands of MoS_2 and WS_2 is almost identical at the band edge, and d-electrons of Mo and W have equal contributions to the valence band edge of $W_{0.5}Mo_{0.5}S_2$. The composition of the conduction bands of MoS_2 and WS_2 is quite different at the band edge, and d-electrons of Mo have major contributions to the conduction band of $W_{0.5}Mo_{0.5}S_2$. A quantified analysis of PDOS is provided in Table S5 of the SI.

transistors. The hole effective mass decreases linearly as the W composition increases, so the hole mobility is likely to be enhanced.

In FETs, the main carrier type for transport is to a large extent decided by the relative position of the metal work function (WF) of source/drain electrodes and the energy level of frontier orbitals of semiconductors in the channel. The transistor usually exhibits n-type conduction if the LUMO level of semiconductor is closer to the Fermi level of metal electrode (the Fermi level E_F = -WF); otherwise it exhibits p-type conduction. Here we examined four common metal electrode materials (Au, WF = 5.2 eV; Ag, WF = 4.2 eV; Cu, WF = 4.6 eV; Pd, WF = 5.12 eV), and compared their Fermi levels with the frontier orbital levels of $W_xMo_{1-x}S_2$ with different W compositions x. The absolute levels of HOMO and LUMO in $W_xMo_{1-x}S_2$ monolayer alloys were determined by the method of vacuum level calibration as described above, and they were plotted as a function of W compositions in Figure 5 along with the Fermi levels of Au, Ag, Cu and Pd. We see that the HOMO level rises linearly as W atoms in the alloys increase; instead, the LUMO level exhibits an energy bowing as a function of W composition. So the bandgap bowing effect in $W_xMo_{1-x}S_2$ monolayer alloys originates from the bowing of LUMO level. The energy level shift of HOMO and LUMO with increasing W composition is in line with the effective mass change of holes and electrons demonstrated above. The results shown in Figure 5 tell us that (i) for Ag and Cu electrodes, the LUMO level of $W_xMo_{1-x}S_2$ alloys is located closer to the Femi level of electrodes and therefore more conducive to electron injection, so the main carrier type should always be electrons in this case no matter what the W composition is; (ii) for Au and Pd electrodes, when the W composition is low, the LUMO level is closer to the Fermi level of Au and Pd, and the $W_xMo_{1-x}S_2$ monolayer exhibits an n-type conductivity; when x is above ~0.13 the main carrier type changes from electrons to holes
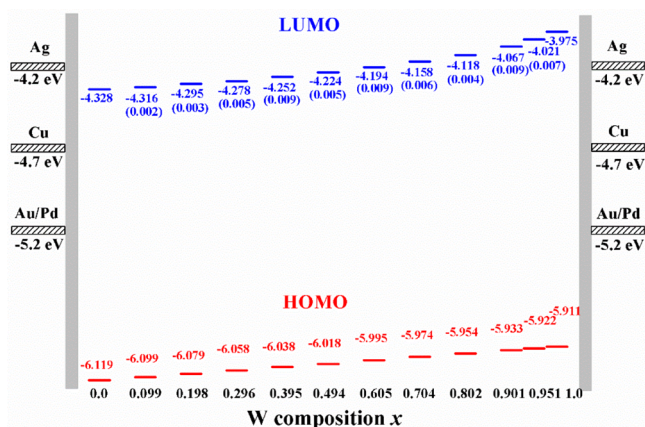
Figure 5. The absolute energy level of HOMO and LUMO for $W_xMo_{1-x}S_2$ monolayer alloys as a function of W composition x. The number in the bracket is the error bar of the LUMO energy. The error bar of the HOMO energy is on the order of 10^{-4}. The frontier orbital energies are compared to the Fermi levels of four metal electrode materials: Au, Ag, Cu and Pd. It is noted that with Au or Pd as electrode, the conduction polarity in FETs is likely to change from n-type to p-type with increasing W composition.

and the 2D alloys exhibit a p-type conductivity. This suggests that when W is mixed into MoS_2 the conduction polarity could change from n-type to p-type in FETs with high work function electrodes, and at certain compositions ambipolar transport is possible. In combination with our finding that the hole effective mass decreases when the W composition increases, we conclude that mixing W into MoS_2 has a positive effect on the hole transport. We need to point out here that the alloy scattering and impurity scattering effects, which are beyond the scope of this work, could also affect carrier mobilities in alloy systems[36−38] and should be further addressed.

In fact, FETs made with chemically synthesized multilayer WS_2 as well as exfoliated thin flakes of WS_2 have been recently realized,[39,40] which demonstrated ambipolar behavior and a high ($\sim 10^5$) on/off current ratio at room temperature. Moreover, the WSe_2 bulk crystals were reported to show a mobility up to 500 cm^2 V^{-1} s^{-1} for p-type conductivity at room temperature and ambipolar behavior at low temperature.[41] Recently, high-performance single layered WSe_2 p-FETs with chemically doped contacts have been reported.[42] A high hole mobility of $\sim$250 cm^2 V^{-1} s^{-1} and current on/off ratio of >10^6 at room temperature were achieved by lowering the contact resistance for hole injection using high work function Pd contacts and degenerate surface doping of the contacts by patterned NO_2 chemisorption on WSe_2. By contrast, lower work function metal contacts such as Ti resulted in ambipolar transport behavior with low current levels owing to high Schottky barrier heights to both CB and VB of WSe_2. A systematic selection of the contact metal toward the design of high-performance n-type monolayer WSe_2 FETs has been demonstrated.[43] It was found that In electrode, among others (Ti, Ag, and Al), leads to small ohmic contact resistance with WSe_2 and an electron mobility of 142 cm^2 V^{-1} s^{-1} at room temperature. These experiments demonstrate how the conduction polarity in FETs changes with the selection of metal electrod materials. We show that the absolute energy levels of frontier orbitals in 2D TMDs can be tuned by alloying, and the conduction polarity of alloys is tunable.

Above all, we have demonstrated that both the effective mass and the conduction polarity are tunable by mixing MoS_2 and WS_2, but due to identical contributions of metal d-electrons to the HOMO whereas different contributions of metal d-electrons to the LUMO for MoS_2 and WS_2, mixing W into MoS_2 benefits the hole transport instead of the electron transport. Other 2D TMD alloys have also been theoretically studied, for example, the stability of $MoS_{2x}Se_{2(1-x)}$ monolayer alloys was discussed recently. Such alloys are predicted to be thermodynamically stable and to be manufactured using CVD or exfoliated from the bulk mixed materials.[44,45] One of works also predicted tunable bandgaps in the mixed compounds, but detailed analysis of electronic properties were not conducted. Our preliminary calculations show that MoS_2 and $MoSe_2$ have almost identical compositions for both HOMO and LUMO, and the effective masses of electrons and holes of $MoSe_2$ are both slightly larger than those of MoS_2. It seems to suggest that mixing in the chalcogen sublattice is a less effective way in engineering the electronic properties of TMDs than mixing in the metal sublattice, because the metal d-electrons have more significant contributions to the frontier orbitals of alloys than the chalcogen p-electrons.

Finally, we present a brief discussion of the stability of 2D $W_xMo_{1-x}S_2$ alloys with different W compositions. The free energy and internal energy of mixing per primitive cell for the alloys were calculated following the work of Komsa et al.[44] and plotted as a function of W composition at 300 K (Figure S3 of the SI). In our calculations the experimental lattice constant of 2H-MoS_2 was used for all compositions of the alloys, but the general trend of the free energies and internal energies is consistent with that of Komsa et al.: the internal energies of mixing are negative for all random configurations, and the free energies of mixing are more negative than the corresponding internal energies due to the favorable entropy change of mixing. These results demonstrated that $W_xMo_{1-x}S_2$ monolayers are thermodynamically stable. In most cases, the formation energy of semiconductor alloys is positive due to the large lattice mismatch between the constituents. Here, the lattice constants of MoS_2 and WS_2 are very close ($\sim$ 0.2%), and we expect the the strain energy in their alloys is negligible. In our calculations, the negative internal mixing energy is only due to the charge exchange. According to the Madelung energy model, the sign of charge exchange enthalpy for a ternary alloy depends on the additional charge exchange.[45,46] Our internal mixing energy is only −4 meV, which indicates that the charge exchange in the alloys is small. Overall, the foramtion of $W_xMo_{1-x}S_2$ alloys can be attributed to the tiny lattice mismatch and the additional charge exchange. In fact, 2D $W_xMo_{1-x}S_2$ alloys have been successfully manufactured through exfoliation from the bulk mixed materials recently.[21]

To summarize, we have investigated the electronic properties of 2D $W_xMo_{1-x}S_2$ alloys with different W compositions x based on first-principles calculations. The free energies of mixing are negative for these monolayer alloys, indicating that they are thermodynamically stable at the room temperature. Interestingly, the hole effective mass of alloys decreases linearly with increasing W composition, and the electron effective mass is always larger than that of MoS_2 or WS_2 monolayer, due to (i) almost identical orbital compositions of HOMO for MoS_2 and WS_2, and very different orbital compositions of LUMO; (ii) both HOMO and LUMO levels of MoS_2 are lower than those of WS_2. This finding suggests that mixing of W atoms into MoS_2 does not favor the electron conduction, and it could

enhance the hole mobility instead. In addition, the main carrier type for transport in FETs could change from electrons to holes with increasing W composition in the alloys due to that the high WF of Au and Pd in the source and drain electrodes is closer to the lifted HOMO level of the alloys. Combining these two findings, we conclude that 2D alloys of MoS_2/WS_2 exhibit better p-type conductivity than MoS_2 and at certain alloy compositions ambipolar behavior is likely to show up. The tunable electronic properties of 2D TMD alloys could open new opportunities for them to be used in electronic and optoelectronic devices.

■ ASSOCIATED CONTENT

Ⓢ Supporting Information

SOC and convergence tests; electron (hole) effective mass for $W_xMo_{1-x}S_2$ monolayer alloys at eight random configurations and with different W compositions; absolute energy levels, PDOS analysis, and charge density distribution of HOMO and LUMO for MoS_2, $W_{0.5}Mo_{0.5}S_2$, and WS_2; internal energies and free energies of mixing for $W_xMo_{1-x}S_2$ monolayer alloys at different W compositions. This material is available free of charge via the Internet at http://pubs.acs.org.

■ AUTHOR INFORMATION

Corresponding Authors
*E-mail: dong913@tsinghua.edu.cn.
*E-mail: zgshuai@tsinghua.edu.cn.
Notes
The authors declare no competing financial interest.

■ ACKNOWLEDGMENTS

■ REFERENCES

(1) Butler, S. Z.; Hollen, S. M.; Cao, L.; Cui, Y.; Gupta, J. A.; Gutiérrez, H. R.; Heinz, T. F.; Hong, S. S.; Huang, J.; Ismach, A. F.; et al. Progress, Challenges, and Opportunities in Two-Dimensional Materials Beyond Graphene. *ACS Nano* **2013**, *7*, 2898–2926.

(2) Wang, Q. H.; Kalantar-Zadeh, K.; Kis, A.; Coleman, J. N.; Strano, M. S. Electronics and Optoelectronics of Two-Dimensional Transition Metal Dichalcogenides. *Nat. Nanotechnol.* **2012**, *7*, 699–712.

(3) Chhowalla, M.; Shin, H. S.; Eda, G.; Li, L.-J.; Loh, K. P.; Zhang, H. The Chemistry of Two-Dimensional Layered Transition Metal Dichalcogenide Nanosheets. *Nat. Chem.* **2013**, *5*, 263–275.

(4) Mak, K. F.; He, K.; Shan, J.; Heinz, T. F. Control of Valley Polarization in Monolayer MoS_2 by Optical Helicity. *Nat. Nanotechnol.* **2012**, *7*, 494–498.

(5) Mak, K. F.; Lee, C.; Hone, J.; Shan, J.; Heinz, T. F. Atomically Thin MoS_2: A New Direct-Gap Semiconductor. *Phys. Rev. Lett.* **2010**, *105*, 136805–136805–4.

(6) Radisavljevic, B.; Radenovic, A.; Brivio, J.; Giacometti, V.; Kis, A. Single-Layer MoS_2 Transistors. *Nat. Nanotechnol.* **2011**, *6*, 147–150.

(7) Zeng, Z.; Yin, Z.; Huang, X.; Li, H.; He, Q.; Lu, G.; Boey, F.; Zhang, H. Single-Layer Semiconducting Nanosheets: High-Yield Preparation and Device Fabrication. *Angew. Chem., Int. Ed.* **2011**, *50*, 11093–11097.

(8) Liu, K.-K.; Zhang, W.; Lee, Y.-H.; Lin, Y.-C.; Chang, M.-T.; Su, C.-Y.; Chang, C.-S.; Li, H.; Shi, Y.; Zhang, H.; et al. Growth of Large-Area and Highly Crystalline MoS_2 Thin Layers on Insulating Substrates. *Nano Lett.* **2012**, *12*, 1538–1544.

(9) Shi, Y.; Zhou, W.; Lu, A.-Y.; Fang, W.; Lee, Y.-H.; Hsu, A. L.; Kim, S. M.; Kim, K. K.; Yang, H. Y.; Li, L.-J.; et al. van der Waals Epitaxy of MoS_2 Layers Using Graphene as Growth Templates. *Nano Lett.* **2012**, *12*, 2784–2791.

(10) Lee, Y.-H.; Zhang, X.-Q.; Zhang, W.; Chang, M.-T.; Lin, C.-T.; Chang, K.-D.; Yu, Y.-C.; Wang, J. T.-W.; Chang, C.-S.; Li, L.-J.; et al. Synthesis of Large-Area MoS_2 Atomic Layers with Chemical Vapor Deposition. *Adv. Mater.* **2012**, *24*, 2320–2325.

(11) Wang, X.; Feng, H.; Wu, Y.; Jiao, L. Controlled Synthesis of Highly Crystalline MoS_2 Flakes by Chemical Vapor Deposition. *J. Am. Chem. Soc.* **2013**, *135*, 5304–5307.

(12) Splendiani, A.; Sun, L.; Zhang, Y.; Li, T.; Kim, J.; Chim, C.-Y.; Galli, G.; Wang, F. Emerging Photoluminescence in Monolayer MoS_2. *Nano Lett.* **2010**, *10*, 1271–1275.

(13) Kuc, A.; Zibouche, N.; Heine, T. Influence of Quantum Confinement on the Electronic Structure of the Transition Metal Sulfide TS_2. *Phys. Rev. B* **2011**, *83*, 245213–245213–4.

(14) Novoselov, K. S.; Geim, A. K.; Morozov, S. V.; Jiang, D.; Zhang, Y.; Dubonos, S. V.; Grigorieva, I. V.; Firsov, A. A. Electric Field Effect in Atomically Thin Carbon Films. *Science* **2004**, *306*, 666–669.

(15) Yoon, Y.; Ganapathi, K.; Salahuddin, S. How Good Can Monolayer MoS_2 Transistors Be? *Nano Lett.* **2011**, *11*, 3768–3773.

(16) Yun, W. S.; Han, S. W.; Hong, S. C.; Kim, I. G.; Lee, J. D. Thickness and Strain Effects on Electronic Structures of Transition Metal Dichalcogenides: 2H-MX_2 Semiconductors (M = Mo, W; X = S, Se, Te). *Phys. Rev. B* **2012**, *85*, 033305–033305–5.

(17) Radisavljevic, B.; Kis, A. Reply to 'Measurement of Mobility in Dual-Gated MoS_2 Transistors'. *Nat. Nanotechnol.* **2013**, *8*, 147–148.

(18) Jena, D.; Konar, A. Enhancement of Carrier Mobility in Semiconductor Nanostructures by Dielectric Engineering. *Phys. Rev. Lett.* **2007**, *98*, 136805–136805–4.

(19) Kaasbjerg, K.; Thygesen, K. S.; Jacobsen, K. W. Phonon-Limited Mobility in n-Type Single-Layer MoS_2 from First Principles. *Phys. Rev. B* **2012**, *85*, 115317–115317–16.

(20) Li, X. D.; Mullen, J. T.; Jin, Z. H.; Borysenko, K. M.; Nardelli, M. B.; Kim, K. W. Intrinsic Electrical Transport Properties of Monolayer Silicene and MoS_2 from First Principles. *Phys. Rev. B* **2013**, *87*, 115418-1–115418-9.

(21) Dumcenco, D. O.; Kobayashi, H.; Liu, Z.; Huang, Y.-S.; Suenaga, K. Visualization and Quantification of Transition Metal Atomic Mixing in $Mo_{1-x}W_xS_2$ Single Layers. *Nat. Commun.* **2013**, *4*, 1351–1351–5.

(22) Chen, Y.; Xi, J.; Dumcenco, D. O.; Liu, Z.; Suenaga, K.; Wang, D.; Shuai, Z.; Huang, Y.-S.; Xie, L. Tunable Band Gap Photoluminescence from Atomically Thin Transition-Metal Dichalcogenide Alloys. *ACS Nano* **2013**, *7*, 4610–4616.

(23) Popescu, V.; Zunger, A. Effective Band Structure of Random Alloys. *Phys. Rev. Lett.* **2010**, *104*, 236403–236403–4.

(24) Kohn, W.; Sham, L. J. Self-Consistent Equations Including Exchange and Correlation Effects. *Phys. Rev.* **1965**, *140*, A1133–A1138.

(25) Blöchl, P. E. Projector Augmented-Wave Method. *Phys. Rev. B* **1994**, *50*, 17953–17979.

(26) Kresse, G.; Joubert, D. From Ultrasoft Pseudopotentials to the Projector Augmented-Wave Method. *Phys. Rev. B* **1999**, *59*, 1758–1775.

(27) Kresse, G.; Hafner, J. Ab initio Molecular Dynamics for Liquid Metals. *Phys. Rev. B* **1993**, *47*, 558–561.

(28) Kresse, G.; Furthmüller, J. Efficient Iterative Schemes for ab initio Total-Energy Calculations Using a Plane-Wave Basis Set. *Phys. Rev. B* **1996**, *54*, 11169–11186.

(29) Zhu, Z. Y.; Cheng, Y. C.; Schwingenschlögl, U. Giant Spin-Orbit-Induced Spin Splitting in Two-Dimensional Transition-Metal Dichalcogenide Semiconductors. *Phys. Rev. B* **2011**, *84*, 153402–153402–5.

(30) Kośmider, K.; Fernández-Rossier, J. Electronic Properties of the MoS_2-WS_2 Heterojunction. *Phys. Rev. B* **2013**, *87*, 075451–075451–4.

(31) Bernard, J. E.; Zunger, A. Electronic Structure of ZnS, ZnSe, ZnTe, and Their Pseudobinary Alloys. *Phys. Rev. B* **1987**, *36*, 3199–3228.

(32) Wei, S.-H.; Zunger, A. Giant and Composition-Dependent Optical Bowing Coefficient in GaAsN Alloys. *Phys. Rev. Lett.* **1996**, *76*, 664−667.

(33) Podberezskaya, N. V.; Magarill, S. A.; Pervukhina, N. V.; Borisov, S. V. Crystal Chemistry of Dichalcogenides MX_2. *J. Struct. Chem.* **2001**, *42*, 654−681.

(34) Sgiarovello, C.; Binggeli, N.; Baldereschi, A. Influence of Surface Morphology on the Si(100) and (111) Ionization Potentials. *Phys. Rev. B* **2001**, *64*, 195305-1−195305-7.

(35) Fall, C. J.; Binggeli, N.; Baldereschi, A. Deriving Accurate Work Functions from Thin-Slab Calculations. *J. Phys.: Condens. Matter* **1999**, *11*, 2689−2696.

(36) Harrison, J.; Hauser, J. Theoretical Calculations of Electron Mobility in Ternary III-V Compounds. *J. Appl. Phys.* **1976**, *47*, 293−300.

(37) Fischetti, M. V.; Laux, S. E. Band Structure, Deformation Potentials, and Carrier Mobility in Strained Si, Ge, and SiGe Alloys. *J. Appl. Phys.* **1996**, *80*, 2234−2252.

(38) Vaughan, M. P.; Murphy-Armando, F.; Fahy, S. First-Principles Investigation of the Alloy Scattering Potential in Dilute $Si_{1-x}C_x$. *Phys. Rev. B* **2012**, *85*, 165209−165209−10.

(39) Braga, D.; Gutiérrez Lezama, I.; Berger, H.; Morpurgo, A. F. Quantitative Determination of the Band Gap of WS_2 with Ambipolar Ionic Liquid-Gated Transistors. *Nano Lett.* **2012**, *12*, 5218−5223.

(40) Sik Hwang, W.; Remskar, M.; Yan, R.; Protasenko, V.; Tahy, K.; Doo Chae, S.; Zhao, P.; Konar, A.; Xing, H.; Seabaugh, A.; et al. Transistors with Chemically Synthesized Layered Semiconductor WS_2 Exhibiting 10^5 Room Temperature Modulation and Ambipolar Behavior. *Appl. Phys. Lett.* **2012**, *101*, 013107−013107−4.

(41) Podzorov, V.; Gershenson, M. E.; Kloc, C.; Zeis, R.; Bucher, E. High-Mobility Field-Effect Transistors Based on Transition Metal Dichalcogenides. *Appl. Phys. Lett.* **2004**, *84*, 3301−3303.

(42) Fang, H.; Chuang, S.; Chang, T. C.; Takei, K.; Takahashi, T.; Javey, A. High-Performance Single Layered WSe_2 p-FETs with Chemically Doped Contacts. *Nano Lett.* **2012**, *12*, 3788−3792.

(43) Liu, W.; Kang, J.; Sarkar, D.; Khatami, Y.; Jena, D.; Banerjee, K. Role of Metal Contacts in Designing High-Performance Monolayer n-Type WSe_2 Field Effect Transistors. *Nano Lett.* **2013**, *13*, 1983−1990.

(44) Komsa, H.-P.; Krasheninnikov, A. V. Two-Dimensional Transition Metal Dichalcogenide Alloys: Stability and Electronic Properties. *J. Phys. Chem. Lett.* **2012**, *3*, 3652−3656.

(45) Kang, J.; Tongay, S.; Li, J.; Wu, J. Monolayer Semiconducting Transition Metal Dichalcogenide Alloys: Stability and Band Bowing. *J. Appl. Phys.* **2013**, *113*, 143703−143703−7.

(46) Ferreira, L. G.; Wei, S.-H.; Zunger, A. First-Principles Calculation of Alloy Phase Diagrams: The Renormalized-Interaction Approach. *Phys. Rev. B* **1989**, *40*, 3197−3231.